J Mater Sci (2013) 48:4671–4680
DOI 10.1007/s10853-012-7061-3

NANOSTRUCTURED MATERIALS

Evolution of microhardness and microstructure in a cast Al–7 % Si alloy during high-pressure torsion

Tarang Mungole · Naresh Nadammal · Kunal Dawra · Praveen Kumar · Megumi Kawasaki · Terence G. Langdon

Received: 10 November 2012 / Accepted: 30 November 2012 / Published online: 13 December 2012

Abstract Disks of a cast Al–7 % Si alloy were processed through high-pressure torsion (HPT) for 1/4, 1/2, 1, 5, and 10 revolutions under a pressure of 6.0 GPa and at temperatures of 298 and 445 K. The hardness of the samples after processing was significantly higher than in the cast sample, and the hardness profiles across the samples became more uniform with increasing numbers of turns. Processing at higher temperature gave lower hardness values. Experiments were conducted to examine the effects of HPT processing on various microstructural aspects of the cast Al–7 % Si alloy such as the grain size, the Taylor factor, and the fraction of high-angle grain boundaries. The results demonstrate that there is a correlation between trends in the microhardness values and the observed microstructures.

T. Mungole · N. Nadammal · P. Kumar (✉)
Department of Materials Engineering, Indian Institute of Science, Bangalore, India
e-mail: praveenk@materials.iisc.ernet.in

K. Dawra
Metallurgical Engineering Department, Institute of Technology, Banaras Hindu University, Varanasi, India

M. Kawasaki
Division of Materials Science and Engineering, Hanyang University, 17 Haengdang-dong, Seongdong-gu, Seoul 133-791, South Korea

M. Kawasaki · T. G. Langdon
Departments of Aerospace & Mechanical Engineering and Materials Science University of Southern California, Los Angeles, CA 90089-1453, USA

T. G. Langdon
Materials Research Group, Faculty of Engineering and the Environment, University of Southampton, Southampton SO17 1BJ, UK

Introduction

Severe plastic deformation (SPD) techniques, such as high-pressure torsion (HPT), equal-channel angular pressing (ECAP), accumulative roll bonding (ARB), and friction stir welding (FSW), are widely employed to significantly refine the grains by imparting large plastic strains to the material [1–5]. These SPD processes represent the top-down approach for producing ultrafine-grained (UFG) materials [6] where grain sizes of a few micrometers to tens of nanometers have been successfully produced in relatively large bulk materials, including materials which are otherwise difficult to process using conventional mechanical forming techniques such as tungsten [7] and tantalum [8]. The UFG materials not only show high strength at low temperatures according to the Hall–Petch relationship, but also they often exhibit superplasticity at moderately high temperatures ($\sim 0.5T_m$ where T_m is the absolute melting temperature). Interestingly, SPD-processed UFG materials also show high strain rate superplasticity at relatively lower temperatures, where this phenomenon is attributed to the presence of very high densities of dislocations in the grains and at the grain boundaries [9–12]. Since one of the key aspects of an SPD process is strain accumulation and HPT is one of the most rapid methods for imposing a high strain in a material [13, 14], there are considerable possibilities for tuning the "microstructure–mechanical behavior" relationship of structural materials through HPT.

Cast Al–Si hypoeutectic alloys are widely used in the automotive industry. The addition of Si up to the eutectic composition (i.e., ~ 12 wt% Si) lowers the melting

temperature of the alloy leading to better control of the casting process and hence microstructural uniformity. Generally, the ultimate tensile strength, the yield strength and the hardness of the as-cast hypoeutectic Al–Si alloys increase, and the ductility (and fatigue life) decreases with an increase in the Si content [15]. Also, the wear rate under high load rapidly decreases with an increase in the Si content; however, the decrease in the wear rate considerably slows down around and above 7 wt% Si and a minima is achieved near the eutectic composition [16]. Therefore, Al–7 wt% Si, as compared with other hypoeutectic Al–Si alloys, may have the optimum combination of the microstructural uniformity, ductility (fatigue life), mechanical strength, and wear resistance; these properties confirm the Al–7 % Si alloy as a very important structural material. The microstructure of the Al–7 % Si hypoeutectic alloy consists primarily of two phases, the primary α-Al phase and a eutectic constituent containing coral-like Si particles embedded within an Al matrix [17]. The effects of ECAP and FSW on the microstructural evolution and mechanical behavior of the cast Al–7 wt% Si have been extensively reported [18–21]. Processing through various routes of ECAP and FSW led to a decrease in the grain size [18–21] and an increase in the elongation to failure of the material [21]. Also, a redistribution of Si particles in the Al matrix was reported following ECAP and FSW [19–21], but the evidence for the nucleation and growth of Si particles at new locations is not conclusive.

For processing by HPT, a report on the effect of HPT processing on the microstructure of the Al–7 % Si alloy showed a uniform distribution of Si precipitates following five turns at room temperature under an imposed pressure of 6.0 GPa [22, 23]. Although the effect of room temperature HPT processing on the hardness of a hypoeutectic Al–Si alloy, namely Al–2 wt% Si, was previously reported [24], there are no reports on the effect of imposing a very high strain on the evolution of hardness in the Al–7 % Si alloy and this is a particularly important Al–Si alloy. As this material is used widely in engine blocks and pistons, information pertaining to the effect of strain imposition on the hardness, which directly correlates with the wear property of a material, is of critical importance. Furthermore, the effects of the HPT processing temperature on the hardness profile as well as the microstructure of any hypoeutectic Al–Si alloy and Al–7 % Si, in particular, are not known although experiments show this is important in other alloys [25] and undoubtedly it will affect the final grain size of the Al–7 % Si alloy. Accordingly, the present research was undertaken to evaluate the influence of the HPT processing conditions, such as temperature and number of turns, on the hardness and the evolution of the microstructure in the cast Al–7 % Si alloy. A qualitative correlation is presented between microstructural features, such as grain size and the Taylor factor, and the measured microhardness after processing.

Experimental material and procedures

A plate of cast Al–7 % Si hypoeutectic alloy was machined into circular disks of 10 mm diameter and 1 mm thickness. These disks were polished to final thicknesses of $\sim$0.82 mm and then annealed at 445 K ($\sim 0.5T_m$) for 5 h in a vacuum furnace operating at 10^{-4} Torr. This annealing was conducted to relieve any residual stress incurred during machining and to ensure uniformity in the initial microstructure prior to processing. The HPT processing of the annealed samples was carried out at two different temperatures, 298 (room temperature) and 445 K ($\sim 0.5T_m$), by placing the sample between two anvils, applying a uniaxial pressure of 6.0 GPa and then rotating the lower anvil. The basic principles of HPT processing were described earlier [26], and the present experiments were conducted under quasi-constrained conditions [27, 28] where there is a small amount of outflow from the disk during the torsional straining. At each temperature, samples were processed to 1/4, 1/2, 1, 5 and 10 turns of HPT.

In HPT processing, the equivalent von Mises strain, ε, at a point at a distance r from the center of the disk may be calculated using the relationships [4, 29, 30]:

$$\varepsilon = \frac{2}{\sqrt{3}}\frac{\pi N r}{h} \quad \gamma \leq 0.8 \tag{1a}$$

and

$$\varepsilon = \frac{2}{\sqrt{3}}\ln\left[\left(1+\frac{\gamma^2}{4}\right)^{1/2}+\frac{\gamma}{2}\right] \quad \gamma > 0.8, \tag{1b}$$

where N is the number of HPT turns, h is the thickness of the disk, and γ is the shear strain which is given as $2\pi Nr/h$.

After HPT processing, the samples were polished metallographically up to 0.06 μm colloidal silica in order to give a mirror-like finish. The hardness values were recorded following the schematic illustration in Fig. 1, where the locations are shown for the individual hardness measurements. At each point, the Vickers microhardness was recorded using a microhardness tester equipped with a Vickers indenter. Specifically, hardness measurements were taken along eight separate diameters on the surface of the disk. Other than the central point, which is common for all diameters, 10 indentation marks were made on a diameter D_1 (shown as horizontal in Fig. 1) and 8 indentation marks were made on the remaining three diameters, D_2, D_3, and D_4; these points are shown as solid rhombohedra in Fig. 1. All points lying on D_1 were equally spaced with a distance of 0.9 mm between the two nearest

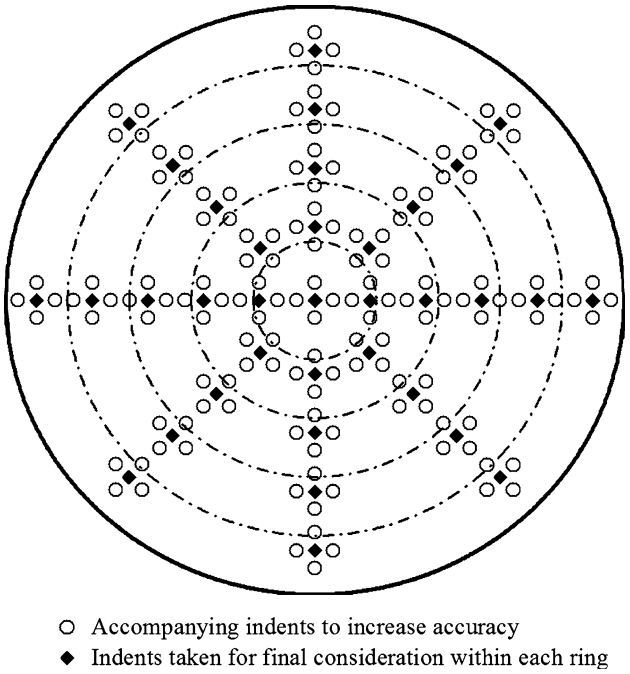

Fig. 1 A schematic illustration showing the indentation marks where the microhardness was measured

neighbors, whereas points on D_2, D_3, and D_4 were placed at distances of ±1.25, ±2.25, ±3.25, and ±4.25 mm from the center of the disk, respectively. Furthermore, four additional indentation marks were also made at a distance of 0.3 mm from each solid rhombohedra point, and these points are shown as open circles in Fig. 1. For statistical accuracy, the hardness at each solid rhombohedral point was calculated by taking an average of the indentation measurements at the solid rhombohedra and the four adjacent open circles. In order to calculate the hardness value as a function of r, and therefore as a function of the distance from the center of the disk, the following procedure was employed: (i) five annular rings were constructed at radial distances of 1, 2, 3, and 4 mm, respectively, (ii) the representative hardness values of all solid rhombohedra situated inside each of the annular rings were averaged, and (iii) the calculated average hardness was then assigned to a point midway from the inner radius and the outer radius of each annular ring. Hence, the hardness values were calculated for distances, r, of ±0.5, ±1.5, ±2.5, ±3.5, and ±4.5 mm, respectively. Therefore, each hardness value at a distance r from the center was calculated from 20 measurements except for $r = 0$ and $r = \pm 0.5$ mm, where it was calculated from 5 and 10 measurements, respectively. Accordingly, it follows that 40 datum points were used for calculating the hardness as a function of equivalent strain.

Microstructural characterization was performed using a scanning electron microscope (SEM) and electron backscatter diffraction (EBSD). Since the shear strain at the center of a disk is zero during the HPT process, much emphasis was placed on conducting microstructural characterization in regions located at $0.5r$ and $0.9r$ from the center. After metallographically polishing up to ~0.25 μm diamond paste, the samples were electro-polished at 232 K using an aqueous solution of 10 % 2-butoxyethanol, 70 % ethanol, and 8 % concentrated perchloric acid for times which depended on the HPT straining conditions but were within the range of 15–90 s. The grain size was determined by calculating the average area of each grain and then equating the area with a circle. The diameter of the circle was then taken as the grain size. Therefore, the reported grain size numbers are very close to those calculated using the mean line intercept method. For the grain size measurements, a region with a misorientation of >5° was assumed to be a grain, and at least 250 grains from a particular region were counted in order to report the representative grain size. These calculations were conducted using the "Grain Size (Diameter)" feature in the TSL OIM software.

Following SEM and EBSD analysis, the Taylor factor and the fraction of the high-angle grain boundaries (HAGB) were calculated using TSL OIM software. Similar to the grain size measurement, at least 250 grains were considered for an EBSD data analysis. The clean-up procedure consisted of grain dilation with a 5° grain tolerance angle and varying minimum grain sizes from 1 to 4 μm depending on the grain size of the sample. The HAGB fractions were calculated by generating grain boundary maps considering HAGBs to have misorientation angles, θ, of >15°. Boundaries with angles between 3 and 15° were considered as low-angle boundaries. The Taylor factor was calculated by taking weighted averages of Taylor factors for all the orientations present in the Taylor factor map. At least five such scans, each consisting of at least 50 grains, were taken from every region to improve the statistical accuracy. The Taylor factor was calculated by assuming a uniaxial compression deformation gradient tensor along the z-axis of the disk in the axial direction.

Results and discussion

Figure 2 shows representative micrographs from the Si particle-rich regions of the Al–7 % Si samples after processing by HPT at 445 K for (a) 1/4 turn (low magnification), (b) 1/4 turn (high magnification), (c) 5 turns (high magnification), and (d) 10 turns (low magnification). As is evident from Fig. 2a, b, large Si particles were concentrated only in certain regions after 1/4 HPT turn and large regions of the α-Al phase remained relatively free of Si particles. However, as shown in Fig. 2c, d, the dispersion of new and small Si precipitates initiated in the α-Al phase

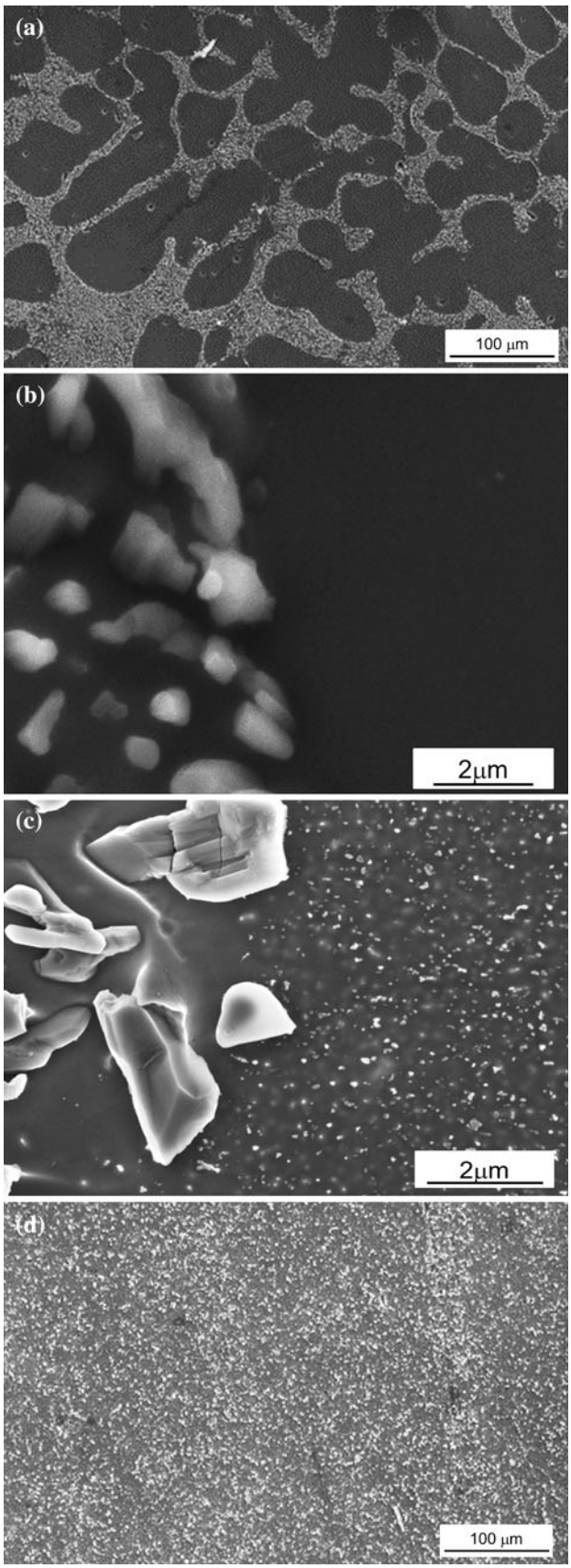

Fig. 2 Representative SEM micrographs showing the distribution of Si precipitates after **a** ¼ turn (*low magnification*), **b** ¼ turn (*high magnification*), **c** 5 turns (*high magnification*), and **d** 10 turns (*low magnification*) of HPT processing at 445 K. All micrographs represent regions at half-radius distance from the center of the disk

with increasing numbers of HPT turns and the distribution of Si particles in the material also became more uniform. This observation of new and small Si precipitates is consistent with earlier work reporting Si precipitation after five turns of HPT conducted at room temperature under a pressure of 6.0 GPa [22].

The formation of these new and small Si particles may have the following two origins: (i) nucleation and growth of new Si precipitates due to an increase in the sample temperature during HPT processing, or (ii) fragmentation of large Si particles into small segments followed by their redistribution in the Al matrix due to the subsequent plastic deformation. It is well established that the temperature of the sample increases from a few tens of degrees to a few hundreds of degrees during HPT processing [22, 31–33]. Recently, an experimentally validated FEM-based modeling was conducted to generate a master plot quantifying the increase in the temperature of the work-piece during HPT processing [28]. The following equation can be derived from a best-fit analysis of the reported data:

$$\frac{\Delta T}{\omega\sigma\left(1+0.025\frac{P}{\sigma}\right)} = 13.35 + 25.458[1-\exp(-0.002627(t-9))] \quad (2)$$

where ΔT, ω, σ, and P are the increase in temperature of the work-piece, the rotation speed of the rotating anvil (given in RPM), the flow stress (given in GPa and estimated by dividing hardness by three) and applied pressure (given in GPa), respectively, and t is the time (given in seconds).

Since the master plot was generated for an experimental set-up similar to the one employed in this work, and it was shown to be valid for several metals, including Al, the rise in sample temperature during this work can be estimated from Eq. (2). Applying Eq. (2) for the experimental conditions employed in this work, the maximum rise in the temperature of the samples can be determined as only ~15 °C, which is not as significant as reported in an earlier work on HPT of Al–7 % Si alloy [22]. It follows that the temperature rise during HPT may have only a limited role in the nucleation and growth of new and small Si particles in this study. Therefore, the fragmentation of large Si particles followed by their redistribution during the continued SPD appears to play the significant role in the dispersal of the new and small Si particles in these HPT processed samples.

Figure 3 shows the variation of the grain size in the α-Al matrix as a function of the equivalent von Mises strain during HPT processing at 298 and 445 K. Since the grain size of samples subjected to SPD processing depends primarily on the magnitude of the imposed strain and the processing temperature, it is appropriate to represent the grain size variation at a selected processing temperature as a function of the equivalent strain. The appropriate strain at the point corresponding to the grain size investigation is readily calculated using Eq. (1a) and (1b).

In Fig. 3, the grain sizes of the samples processed at room temperature, corresponding to low temperature processing, were consistently smaller than for the samples processed at the higher temperature of 445 K. Furthermore, close inspection of Fig. 3 shows that the grain size evolution in Al–7 % Si samples during HPT processing is readily divisible into three distinct stages: (i) at low imposed strains, henceforth termed stage I, the grain sizes rapidly decrease by a factor of ~175 and ~125 at 298 and 445 K, respectively, (ii) at intermediate imposed strains in stage II, the grain sizes remain essentially constant with increasing equivalent strain, and (iii) at very large strains in stage III, the grain size decreases further with imposed strain although this latter stage was observed only in the samples processed at the low temperature.

In addition to the differences in the grain size, the effect of the HPT processing temperature on the evolution of the grain size in the Al–7 % Si alloy is further highlighted by noting that the rate of decrease in the grain sizes in stage I is faster at the low temperature and stage III is absent at the high temperature. These temperature differences can be attributed to the faster recovery of dislocations at the higher temperature which limits the effect of the imposed strain on the accumulation of dislocations and thereby affects the significance of grain refinement during SPD. Conversely, both of these processes become significant at temperatures greater than $\sim 0.5T_m$. The presence of stage III in the samples processed at the low temperature suggests that the dislocation generation rate due to the imposed strains, and therefore the rate of formation of subgrains, exceeds the recovery rate at this low temperature. It is reasonable to speculate that an exhaustion of the recovery rate by comparison with the dislocation generation rate may occur also at the higher processing temperature, but then a much higher equivalent strain will be required so that it is necessary to process the disk through more than 10 turns.

Figure 4 shows the effect of the HPT processing conditions, specifically the number of turns (or the equivalent strain) and the temperature, on the evolution of hardness in the Al–7 % Si samples. As shown in Fig. 4a, the hardness profiles of the HPT processed samples are symmetrical across the centers of the disks. This is consistent with the

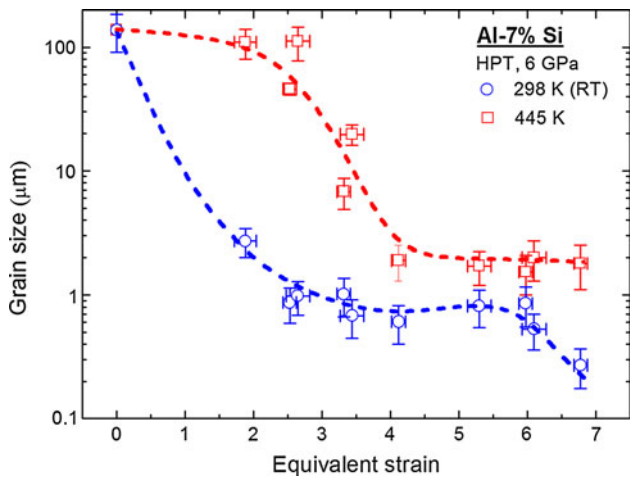

Fig. 3 Variation of grain size with equivalent von Mises strain, ε, following HPT processing at 298 and 445 K: the strain was calculated using Eq. (1a)

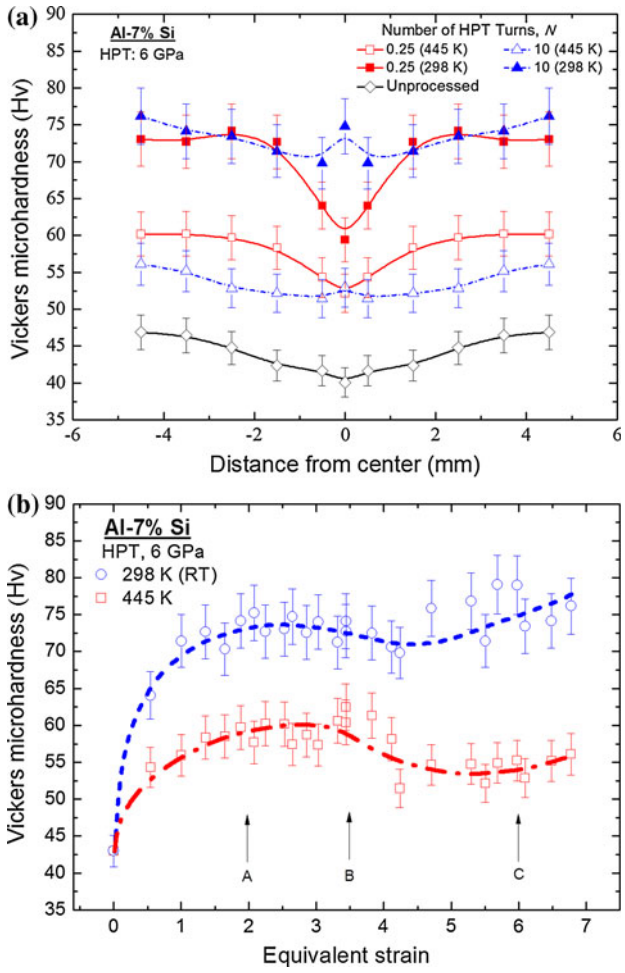

Fig. 4 Vickers microhardness of HPT processed samples with **a** distance from the center of the disk (only a few samples are shown for clarity) and **b** imposed equivalent von Mises strain; the *points A*, *B*, and *C* in **b** indicate the locations for the texture maps shown in Fig. 5

radial hardness symmetry generally associated with HPT processing [24, 34–36] and further justifies the use of strain as the abscissa in Fig. 3 and other plots. At both temperatures, the hardness values of the processed samples are significantly higher than in the unprocessed samples which is again consistent with the general results for most materials processed by HPT [34–36] and is attributed mainly to the grain refinement. Consistent with the differences in the grain sizes between the samples processed at the high temperature and the low temperature, as shown in Fig. 3, the hardness of the samples processed at the low temperature was higher than those processed at the high temperature. At both temperatures, the relatively low numbers of HPT turns led to the lower hardness values in the central regions as compared to the peripheral regions. Figure 4a shows also that the hardness profiles across the disk samples become more uniform with increasing numbers of HPT turns, where this is consistent with a model developed theoretically using strain gradient plasticity modeling [37]. It should be noted that the aforementioned observations of (i) the marginal decrease or no significant change in the hardness values following a very high number of HPT turns, and (ii) the increase in the uniformity of the hardness profile across the sample are in direct contrast with the effects of these HPT parameters on Al–2 % Si as previously reported [24]. Although, a detailed study of the effects of Si addition on the HPT processed Al–Si alloy is warranted to fully understand the above differences between the two Al–Si hypoeutectic alloys, it can be speculated from the available data that the main reason for the above differences lies in the uniform distribution of Si particles, whose volume fraction (as well as number) is much larger in Al–7 % Si alloy as compared to Al–2 % Si, following large numbers of HPT turns (Fig. 2) and, as will be discussed later, the Si particle assisted strain-induced recrystallization of the Al grains.

Figure 4b shows the variation of the hardness as a function of the equivalent von Mises strain and it is apparent that the hardness varies non-monotonically with the imposed strain. This observation also implies that the hardness at a fixed location in a sample does not vary monotonically with the number of HPT turns. At both processing temperatures, the hardness increases rapidly at the beginning of the straining process, and thereafter the rate of increase in the hardness slows down and even slightly decreases before again increasing at very high strains. The initial rapid increase and the subsequent slowing in the rate of increase in hardness of the material may be explained by examining the trend observed in the grain size variation with the imposed strain as shown in Fig. 3. However, the observed decrease in hardness after reaching a maximum value followed by the final increase in hardness is not readily explained by the grain size information, and instead it is necessary to consider the texture. This is because the grain sizes of Al–7 % Si do not increase with strain but, as shown in Fig. 3, they either remain constant with strain at 445 K or decrease further at 298 K.

Figure 5a, b show representative EBSD patterns of the samples processed through HPT at 298 and 445 K, respectively. The images showing texture information were taken at the locations with equivalent strains of 2, 3.5, and 6, and these points are highlighted by the letters “A”, “B” and “C”, respectively, in Fig. 4b. A comparison of Fig. 5a, b shows that the samples processed at the high temperature consist of a high fraction of subgrains at the lower imposed strains, and this is different from the sample processed at the low temperature. This is consistent with the grain size evolution data in Fig. 3 where the grain refinement process at the high temperature is slower because of the faster dislocation recovery rate. Furthermore, the texture map of the samples processed at the low temperature shows a considerable shift from fiber to a random texture following a gradual increase in the imposed strain from 3.5 to 6; in fact, the pole figure of the region with an imposed strain of 6 shows no prominent texture. This demonstrates the occurrence of a strain driven dynamic recrystallization (DRX) during low temperature HPT processing. Since a further strain imposition can induce the formation of new subgrains in the recrystallized grains leading to further grain refinement, the grain size of the samples processed through HPT at the low temperature show a decrease in grain size after a brief period of saturation where this is designated as stages II and III in Fig. 3. This evidence confirms the occurrence of a “grain refinement–recrystallization–grain refinement” cycle in these samples during HPT processing. However, the texture maps of the samples processed at the high temperature show evidence for DRX only at the highest imposed strains and it appears instead that the first cycle of the grain refinement–recrystallization phase is not fully completed in the high temperature samples. If these samples were processed to even higher turns of HPT at the high temperature, it is probable that a further decreases in the grain size would occur.

Figure 6 shows the evolution in the fraction of HAGBs in the Al–7 % Si samples as a function of the imposed strain and the HPT processing temperature. At both temperatures, the fraction of HAGBs initially decreases suggesting the formation of subgrains as a response to the imposed strain. Following the initial decrease, the fraction of HAGBs increases with imposed strain as the existing subgrain boundaries transform into HAGBs to further accommodate the continuous influx of new dislocations. When the fraction of HAGBs becomes close to 70 %, a decrease in the fraction of HAGBs is noted thereby indicating the formation of new subgrains. However, this

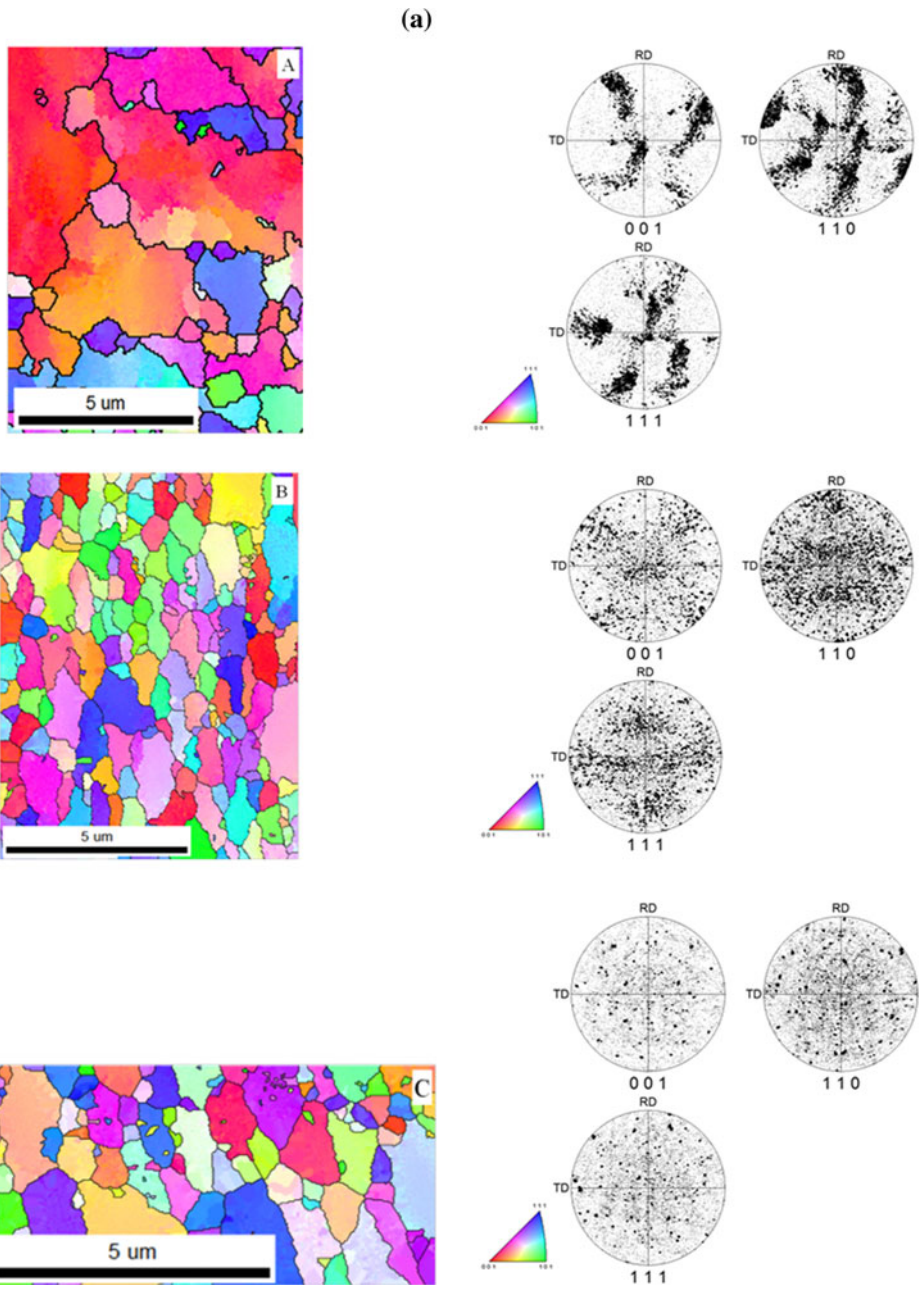

Fig. 5 Inverse pole figure maps and the corresponding discrete pole figures of Al–7 % Si samples processed at **a** 298 K and **b** 445 K; micrographs denoted by *A*, *B*, and *C* correspond to the locations at strains shown in Fig. 4b

decrease is only in the incipient phase during high temperature HPT processing, whereas it is initiated and completed at much smaller strains during low temperature HPT processing. Furthermore, this decrease in the fraction of HAGBs and the subsequent partial increase is also noted in the low temperature samples at the highest strains on the right side of point C in Fig. 6. Thus, the rate of change of the fraction of HAGBs at the high temperature is much slower than at the low temperature; for example, the difference in the strain values where the fractions of HAGBs start to increase after the initial decrease (i.e., the distance between points A and B in Fig. 6) is almost 1.5, and this can be attributed again to the slower rate of dislocation accumulation inside the material at the high temperature due to the associated faster recovery rate. A comparison of Figs. 5 and 6 suggests that an increase in the fraction of HAGBs to a maximum, followed by a decrease, actually corresponds to the occurrence of DRX. Therefore, consistent with the earlier discussion, Fig. 6 also shows that a sample recrystallizes at lower strain if it is processed at a low temperature.

The Taylor factor of the Al–7 % Si samples processed through HPT was calculated from the EBSD data and the result is shown in Fig. 7 as a function of the equivalent von Mises strain. The Taylor factor of the samples processed at both temperatures varies non-monotonically with the

Fig. 5 continued

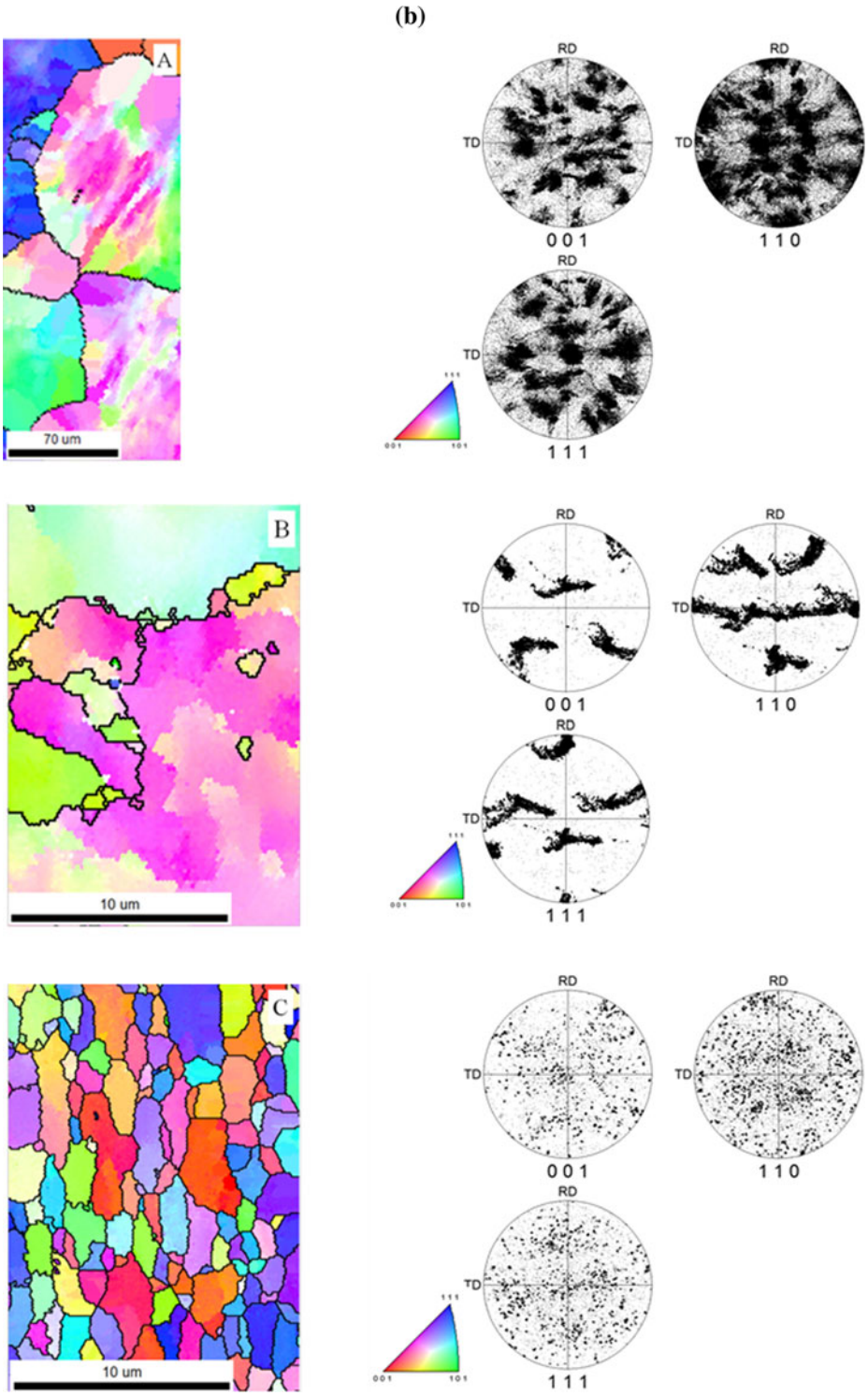

imposed strain but nevertheless there remains an important difference. The Taylor factor of the samples processed at the high temperature initially increases and this is followed by a decrease and finally it increases again with the imposed strain. On the other hand, the Taylor factor of the samples processed at the low temperature initially decreases followed by an increase, and then it becomes essentially saturated to a value similar to that observed in the unprocessed, annealed sample. Since the Taylor factor represents the resistance of a material against plastic deformation [38], the hardness of a material is influenced by the Taylor factor in addition to the Hall–Petch relationship. A comparison of Figs. 3, 4b, and 7 reveals that the decrease in the hardness of the samples processed at the

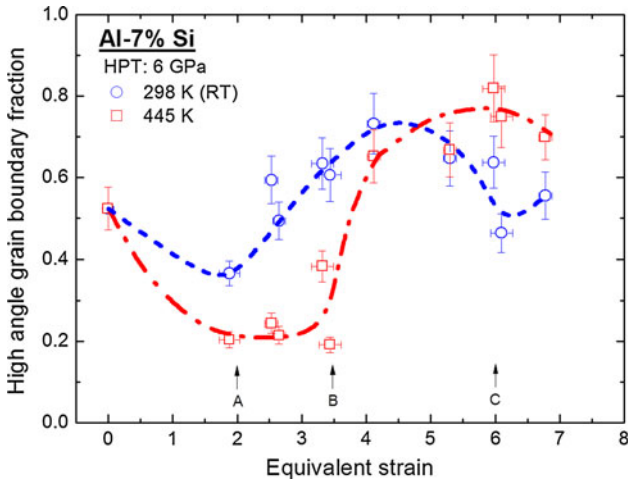

Fig. 6 Fraction of high-angle boundaries as a function of the imposed equivalent von Mises strain; the *points A*, *B*, and *C* indicate the locations for the texture maps shown in Fig. 5

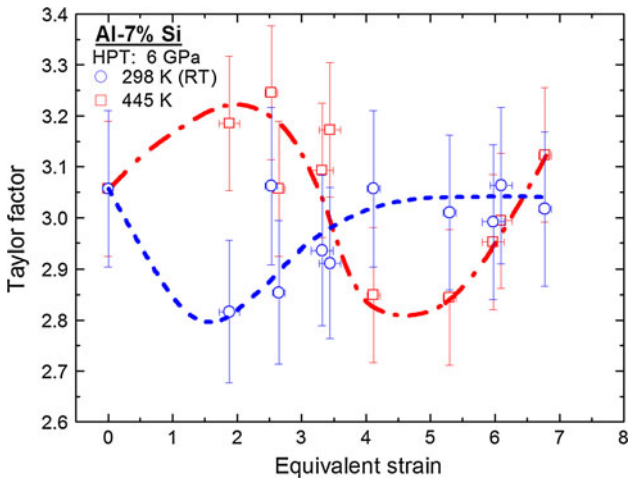

Fig. 7 Effect of the imposed equivalent von Mises strain on the Taylor factor of the cast Al–7 % Si samples processed through HPT

high temperature after reaching a maximum is due to a corresponding decrease in the Taylor factor because the grain size remains constant. Similarly, the ensuing increase in the hardness of the samples at large strains relates directly to the corresponding increase in the Taylor factor.

In addition, the samples processed at the low temperature reveal another important aspect of the evolution of hardness during HPT processing. At low strains, the Taylor factor of the samples processed at the low temperature decreases with the imposed strain, while the hardness of the sample increases. The explanation for this trend lies in the dominant effect of grain refinement in these samples over these imposed strains. Furthermore, the increase in the hardness of the samples processed at the low temperature at high strains, where the Taylor factor became saturated, can now be attributed directly to the decrease in the grain size.

Conclusions

1. The HPT processing of a cast Al–7 % Si alloy was conducted at a low temperature of 298 K and a high temperature of 445 K for various turns. The processing produced UFG materials but the grain sizes of the samples processed at the low temperature were significantly smaller than those processed at the high temperature. In addition, the amount of grain refinement in each HPT turn was more rapid during the low temperature processing.
2. As the number of HPT turns or the imposed strain was increased, the distribution of Si particles became reasonably uniform. Also, new and small Si precipitates were dispersed in the α-Al phase.
3. All processed samples showed significantly higher hardness than the unprocessed cast sample. However, the hardness values of the samples processed at the low temperatures were consistently higher than those processed at the high temperature.
4. The variation of hardness with imposed strain was non-monotonous and this is attributed to a "grain refinement–recrystallization–grain refinement" cycle. During this cycle, the hardness of the sample increases due to strain accumulation but then decreases due to recrystallization which relieves the strain. The non-monotonous variation in hardness with imposed strain may be explained by simultaneously incorporating the effects of grain size hardening due to the Hall–Petch relationship and Taylor factor strengthening.

Acknowledgements This work was partially funded by a Seed Grant (Indian Institute of Science, Bangalore) to PK. The authors would like to thank Dr. Sarath Menon of Naval Postgraduate School, Monterey, CA, USA, for providing the cast Al–7 % Si samples. The work of two of the authors was supported in part by the National Science Foundation of the United States under Grant No. DMR-1160966 and in part by the European Research Council under ERC Grant Agreement No. 267464-SPDMETALS (MK and TGL).

References

1. Saito Y, Utsunomiya H, Tsuji N, Sakai T (1999) Acta Mater 47:579
2. Valiev RZ, Langdon TG (2006) Prog Mater Sci 51:881
3. Valiev RZ, Estrin Y, Horita Z, Langdon TG, Zehetbauer MJ, Zhu YT (2006) JOM 58(4):33
4. Zhilyaev AP, Langdon TG (2008) Prog Mater Sci 53:893
5. Zhu Y, Valiev RZ, Langdon TG, Tsuji N, Lu K (2010) MRS Bull 35:977
6. Zhu YT, Lowe TC, Langdon TG (2004) Scripta Mater 51:825

7. Wei Q, Zhang HT, Schuster BE, Ramesh KT, Valiev RZ, Kecskes LJ, Dowding RJ, Magness L, Cho K (2006) Acta Mater 54:4079
8. Wei Q, Pan ZL, Wu XL, Schuster BE, Kecskes LJ, Valiev RZ (2011) Acta Mater 59:2423
9. Ma Y, Furukawa M, Horita Z, Nemoto M, Valiev RZ, Langdon TG (1996) Mater Trans JIM 37:336
10. Valiev RZ, Salimonenko DA, Tsenev NK, Berbon PB, Langdon TG (1997) Scripta Mater 37:1945
11. Mukai T, Watanabe H, Higashi K (2000) Mater Sci Technol 16:1314
12. Xu C, Furukawa M, Horita Z, Langdon TG (2004) J Alloys Compd 378:27
13. Stolyarov VV, Zhu YT, Lowe TC, Islamgaliev RK, Valiev RZ (1999) Nanostruct Mater 11:947
14. Zhilyaev AP, Kim BK, Nurislamova GV, Baro MD, Szpunar JA, Langdon TG (2002) Scripta Mater 48:575
15. Torabian H, Pathak JP, Tiwari SN (1994) Wear 172:49
16. Clarke J, Sarkar AD (1979) Wear 54:7
17. Warmuzek M (2004) Aluminum–silicon casting alloys: atlas of microfractographs. ASM International, Materials Park
18. García-Infanta JM, Swaminathan S, Zhilyaev AP, Carreño F, Ruano OA, McNelley TR (2008) Mater Sci Eng A 485:160
19. García-Infanta JM, Zhilyaev AP, Cepeda-Jiménez CM, Ruano OA, Carreño F (2008) Scripta Mater 58:138
20. García-Infanta JM, Swaminathan S, Cepeda-Jiménez CM, McNelley TR, Ruano OA, Carreño F (2009) J Alloys Compd 478:139
21. García-Infanta JM, Zhilyaev AP, Carreño F, Ruano OA, Su JQ, Menon SK, McNelley TR (2010) J Mater Sci 45:4613. doi: 10.1007/s10853-010-4530-4
22. Zhilyaev AP, García-Infanta JM, Carreño F, Langdon TG, Ruano OA (2007) Scripta Mater 57:763
23. Cepeda-Jiménez CM, Garía-Infanta JM, Zhilyaev AP, Ruano OA, Carreño F (2011) Mater Sci Eng A528:7938
24. Rajinikanth V, Venkateswarlu K, Sen MK, Das M, Alhajeri SN, Langdon TG (2011) Mater Sci Eng 528A:1702
25. Huang Y, Figueiredo RB, Baudin T, Brisset F, Langdon TG (2012) Adv Eng Mater 14:1018
26. Kawasaki M, Langdon TG (2008) Mater Sci Eng A 498:341
27. Figueiredo RB, Cetlin PR, Langdon TG (2011) Mater Sci Eng A528:8198
28. Figueiredo RB, Pereira PHR, Aguilar MTP, Cetlin PR, Langdon TG (2012) Acta Mater 60:3190
29. Valiev RZ, Ivanisenko YuV, Rauch EF, Baudelet B (1996) Acta Mater 44:4705
30. Degtyarev MV, Chashchukhina TI, Voronova LM, Davydova LS, Pilyugin VP (2000) Phys Metal Metallogr 90:604
31. Todaka Y, Umemoto M, Yamazaki A, Susaki J, Tsuchiya K (2008) Mater Trans 49:7
32. Hóbor S, Kovács Z, Révész Á (2010) J Alloys Compd 495:352
33. Edalati K, Miresmaeili R, Horita Z, Kanayama H, Pippan R (2011) Mater Sci Eng A528:7301
34. Xu C, Horita Z, Langdon TG (2007) Acta Mater 55:203
35. Xu C, Horita Z, Langdon TG (2008) Acta Mater 56:5168
36. Kawasaki M, Figueiredo RB, Langdon TG (2011) Acta Mater 59:308
37. Estrin Y, Molotnikov A, Davies CHJ, Lapovok R (2008) J Mech Phys Solids 56:1186
38. Bunge HJ (1970) Kristall und Technik 5:145